



ARL-TR-8919 • MAR 2020



Control Surface Design Analysis for Munitions

by Joshua T Bryson, Joseph D Vasile, and Frank E Fresconi

Approved for public release; distribution is unlimited.

NOTICES

Disclaimers

The findings in this report are not to be construed as an official Department of the Army position unless so designated by other authorized documents.

Citation of manufacturer's or trade names does not constitute an official endorsement or approval of the use thereof.

Destroy this report when it is no longer needed. Do not return it to the originator.

ARL-TR-8919 • MAR 2020



Control Surface Design Analysis for Munitions

Joshua T Bryson, Joseph D Vasile, and Frank E Fresconi

Weapons and Materials Research Directorate, CCDC Army Research Laboratory

REPORT DOCUMENTATION PAGE				Form Approved OMB No. 0704-0188	
<p>Public reporting burden for this collection of information is estimated to average 1 hour per response, including the time for reviewing instructions, searching existing data sources, gathering and maintaining the data needed, and completing and reviewing the collection information. Send comments regarding this burden estimate or any other aspect of this collection of information, including suggestions for reducing the burden, to Department of Defense, Washington Headquarters Services, Directorate for Information Operations and Reports (0704-0188), 1215 Jefferson Davis Highway, Suite 1204, Arlington, VA 22202-4302. Respondents should be aware that notwithstanding any other provision of law, no person shall be subject to any penalty for failing to comply with a collection of information if it does not display a currently valid OMB control number.</p> <p>PLEASE DO NOT RETURN YOUR FORM TO THE ABOVE ADDRESS.</p>					
1. REPORT DATE (DD-MM-YYYY) March 2020		2. REPORT TYPE Technical Report		3. DATES COVERED (From - To) 1 June–1 November 2019	
4. TITLE AND SUBTITLE Control Surface Design Analysis for Munitions				5a. CONTRACT NUMBER	
				5b. GRANT NUMBER	
				5c. PROGRAM ELEMENT NUMBER	
6. AUTHOR(S) Joshua T Bryson, Joseph D Vasile, and Frank E Fresconi				5d. PROJECT NUMBER	
				5e. TASK NUMBER	
				5f. WORK UNIT NUMBER	
7. PERFORMING ORGANIZATION NAME(S) AND ADDRESS(ES) CCDC Army Research Laboratory ATTN: FCDD-RLW-A Aberdeen Proving Ground, MD 21005				8. PERFORMING ORGANIZATION REPORT NUMBER ARL-TR-8919	
9. SPONSORING/MONITORING AGENCY NAME(S) AND ADDRESS(ES)				10. SPONSOR/MONITOR'S ACRONYM(S)	
				11. SPONSOR/MONITOR'S REPORT NUMBER(S)	
12. DISTRIBUTION/AVAILABILITY STATEMENT Approved for public release; distribution is unlimited.					
13. SUPPLEMENTARY NOTES ORCID ID(s): Joshua T Bryson, 0000-0002-0753-6823; Joseph D Vasile, 0000-0003-3812-6277					
14. ABSTRACT Enhancing munition maneuverability is a key enabling technology for both range extension and terminal maneuvers of long-range precision munitions. One approach to munition maneuverability is to deflect control surfaces to achieve body attack angles that generate lift from the body and other aerodynamic surfaces. This report presents a methodology to analyze aerodynamic control surfaces to determine effectiveness at generating a pitching or yawing moment on a projectile to attain an angle of attack that produces significant lateral accelerations in flight. The methodology demonstrated in this report is for a gun-launched, aerodynamically stabilized, fin-controlled projectile, but is applicable to other control surface design problems.					
15. SUBJECT TERMS fin control, nonlinear aerodynamic model, aerodynamic trim, control surface effectiveness, optimal lift to drag					
16. SECURITY CLASSIFICATION OF: Unclassified			17. LIMITATION OF ABSTRACT UU	18. NUMBER OF PAGES 24	19a. NAME OF RESPONSIBLE PERSON Joshua T Bryson
a. REPORT Unclassified	b. ABSTRACT Unclassified	c. THIS PAGE Unclassified			19b. TELEPHONE NUMBER (Include area code) (410) 306-1939

Contents

List of Figures	iv
List of Tables	iv
1. Introduction	1
2. Airframe	1
3. Aerodynamic Model	3
4. Control Surface Design Methodology	5
5. Conclusion	13
6. References	14
Nomenclature	16
List of Symbols, Abbreviations, and Acronyms	17
Distribution List	18

List of Figures

Fig. 1	Illustration of the projectile's flight body. Dimensions are given in millimeters.	2
Fig. 2	Numbering scheme and deflection sign convention for the trailing-edge control surfaces compared to the body-fixed coordinate system. View is from the projectile base.	3
Fig. 3	Comparison of a) the aerodynamic body coordinate frame for the aerodynamic coefficients and b) the flight dynamics coordinate frame for the calculated forces and moments.....	5
Fig. 4	Total pitching moment, C_m , as well as the FAS and MAS C_m components vs. α for varying δq at Mach 2. The pitch trim α for each δq is found where the total C_m curves cross the $C_m = 0$ line, indicated with red circles.....	6
Fig. 5	Total pitching moment, C_m , as well as the FAS and MAS C_m components vs. α for varying δq for the 8-cm control surface.....	7
Fig. 6	Total pitching moment, C_m , as well as the FAS and MAS C_m components vs. α for varying δq for the 12-cm control surface.....	8
Fig. 7	Total C_m and C_N for 8-cm (a, c, e) and 12-cm (b, d, f) fin-flap data as a function of body angle of attack for α , and pitch deflection, δ , for Mach 0.6 (a, b), 2 (c, d), and 3 (e, f). Lines of constant deflection are solid, while lines of constant angle of attack are dashed.	9
Fig. 8	Comparison of CL and CD at trim for various pitch deflections across Mach. The optimal CL/CD ratio across Mach is plotted in black in a) and b), with the corresponding CL and CD values plotted in black on c), d) and e), f), respectively.	11
Fig. 9	Trim α across Mach for varying pitch deflection angles for both the 8- and 12-cm control surface. The α corresponding to the maximum lift-to-drag is plotted in black.	12
Fig. 10	Pitch deflection schedule across Mach to optimize lift-to-drag ratio for the 8- and 12-cm control surface designs. Both designs achieve similar α to optimize lift-to-drag, but the 12-cm control surface generally requires smaller deflections than the 8-cm design.	13

List of Tables

Table 1	Mass properties for projectile	2
---------	--------------------------------------	---

1. Introduction

Recent emphasis has been placed on investigating technologies and methodologies that can extend the range of guided munitions to provide better coverage of the battlefield. Range extension improvements can be achieved through rocket propulsion and gun propellant technology to increase projectile energy. Interior ballistics and propulsion technology research are being leveraged to extend range through increased launch energy.¹

For a fixed launch energy, the munition range can be extended by enhancing the projectile maneuverability to generate lift through a positive body angle of attack, enabling range extension through gliding flight^{2–4} as well as terminal maneuvers. Projectile maneuverability is influenced by the airframe design and aerodynamics, as well as the design and implementation of control surfaces.^{2–4} Active research into low-drag, high-lift airframes for both supersonic and subsonic flight regimes is improving the understanding of desirable features of the airframe design while reducing design cycle iteration time to rapidly evolve capabilities.⁵

This report presents a methodology to analyze control surface designs and their effect on the projectile, quantifying the ability to generate lift through positive body angle of attack. This research is illustrated on a generic fin-controlled projectile, but the approach is applicable to other control surface design problems. The goal for this projectile illustration problem is to size the control surface to achieve lift-to-drag ratio of 3 across the supersonic and subsonic flight regimes with less than 20° required deflection on each control surface.

2. Airframe

The characteristics of the projectile outer-mold line were shaped through a series of optimization analyses that identified design candidates with low drag and high lift-to-drag ratios.⁵ The optimization study focused on fin-stabilized designs to improve maneuverability of the projectile. The projectile is designed to be sabot-launched from an 8-inch-diameter gun, using a smooth-bore barrel or slip-band obturator. The projectile has no deploying aerodynamic surfaces after launch. The 8-inch-diameter gun requirement constrains the optimization to limit the fin span to 8 inches tip-to-tip. The optimized control surface design for a given body baseline configuration with a 105-mm diameter, 10-caliber length, and ogive length of 30% of the overall length of the projectile is shown in Fig. 1. The design was optimized to maximize lift to drag, minimize drag, and meet a desired static margin value (i.e., 0.3) across supersonic Mach regime ($M = 1–4$) at an 8° body angle attack. This 8° body angle was selected based on preliminary trim angle predictions

for the vehicle with trailing-edge flap deflections. Table 1 shows the projectile's mass properties.

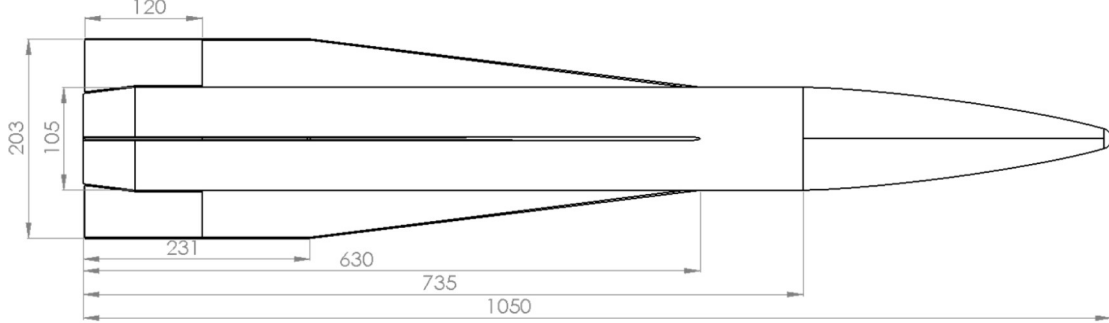


Fig. 1 Illustration of the projectile's flight body. Dimensions are given in millimeters.

Table 1 Mass properties for projectile

Mass properties	
Mass	14.8 kg
CG _X	630 mm from nose
CG _Y , CG _Z	on center line
I _{XX}	0.0273 kg·m ²
I _{YY} , I _{ZZ}	1.17 kg·m ²

A trailing-edge flap on each of the four fins is rotated about the leading edge to provide control of the projectile during flight. Figure 1 shows the trailing-edge flap as 12 cm, but a variant with 8-cm trailing-edge flaps is also considered in this study. The aerodynamic forces and moments of the configuration were obtained using both semi-empirical aerodynamic prediction code Missile DATCOM (release 2014),⁶ as well as NASA's Cartesian Euler computational fluid dynamics (CFD) analysis package Cart3D (1.5.5).⁷ Only the drag and dynamic derivatives for the airframe were predicted using DATCOM, whereas all other forces and moments (e.g., pitching moment of airframe, normal force of trailing-edge flap, and so on) were predicted by Cart3D. The aerodynamic data for the trailing-edge flap components were found by simulating a single trailing-edge flap (i.e., flap 3) in the cruciform orientation at multiple deflections (i.e., $\delta = 0^\circ, 5^\circ, 10^\circ, 15^\circ, 25^\circ$, and 30°) across all flight conditions. The trailing-edge flap data were then applied to the other flaps (i.e., flaps 1, 2, and 4) and combined with the rest of the airframe as discussed in Section 3. The numbering scheme of the control flaps as well as the deflection sign convention is presented in Fig. 2.

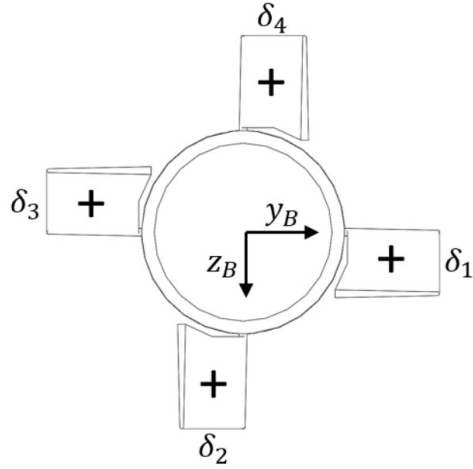


Fig. 2 Numbering scheme and deflection sign convention for the trailing-edge control surfaces compared to the body-fixed coordinate system. View is from the projectile base.

3. Aerodynamic Model

The aerodynamic model provides the aerodynamic forces and moments at a given angle of attack and Mach number using aerodynamic coefficient data.^{8–10} Aerodynamic data describing the forces and moments due to the movable fin tabs, termed movable aerodynamic surfaces (MAS), are applied separately from the aerodynamic data for the assembly of the body and fixed fin surfaces, referred to as fixed aerodynamic surfaces (FAS).

The aerodynamic forces and moments from the FAS component are $[F_X \ F_Y \ F_Z]^T$ and $[M_L \ M_M \ M_N]^T$, respectively, and are given in Eqs. 1–6.

$$F_X = -QS \left[C_{X_0}(M) + C_{X_{\bar{\alpha}^2}}(M) \sin^2 \bar{\alpha} \right] \quad (1)$$

$$F_Y = -QS \left[C_{Y_\beta}(M) \sin \beta + C_{Y_{\beta^3}}(M) \sin^3 \beta + C_{Y_{\beta^5}}(M) \sin^5 \beta \right] \quad (2)$$

$$F_Z = -QS \left[C_{Z_\alpha}(M) \sin \alpha + C_{Z_{\alpha^3}}(M) \sin^3 \alpha + C_{Z_{\alpha^5}}(M) \sin^5 \alpha \right] \quad (3)$$

$$M_L = QSD \left[C_{l_0}(M) + C_{l_p}(M) \frac{pD}{2V} \right] \quad (4)$$

$$M_M = QSD \left[C_{m_\alpha}(M) \sin \alpha + C_{m_{\alpha^3}}(M) \sin^3 \alpha + C_{m_{\alpha^5}}(M) \sin^5 \alpha + C_{m_q}(M) \frac{qD}{2V} \right] \quad (5)$$

$$M_N = QSD \left[-C_{n_\beta}(M) \sin \beta - C_{n_{\beta^3}}(M) \sin^3 \beta - C_{n_{\beta^5}}(M) \sin^5 \beta + C_{n_r}(M) \frac{rD}{2V} \right] \quad (6)$$

where α is the body angle of attack, β is the body angle of sideslip, $\bar{\alpha} = \sqrt{\alpha^2 + \beta^2}$ is the total body angle of attack, D is the projectile diameter, V is the projectile velocity, $Q = \frac{1}{2}\rho V^2$ is the dynamic pressure, and $S = \frac{\pi}{4}D^2$ is the aerodynamic reference area.

The MAS aerodynamic model is given in Eqs. 7–12, which sums the force and moment contributions of the four movable fin-flap surfaces arrayed around the body.

$$F_X^{MAS} = -QS \sum_{i=1}^4 \left[C_{X_0}^i(M, \delta_i) + C_{X_{\bar{\alpha}^2}}^i(M, \delta_i) \sin^2 \bar{\alpha} \right] \quad (7)$$

$$\begin{aligned} F_Y^{MAS} = -QS \sum_{i=1}^4 & \left[C_{Y_\beta}^i(M, \delta_i) \sin \beta + C_{Y_{\beta^3}}^i(M, \delta_i) \sin^3 \beta \right. \\ & \left. + C_{Y_{\beta^5}}^i(M, \delta_i) \sin^5 \beta \right] \end{aligned} \quad (8)$$

$$\begin{aligned} F_Z^{MAS} = -QS \sum_{i=1}^4 & \left[C_{Z_\alpha}^i(M, \delta_i) \sin \alpha + C_{Z_{\alpha^3}}^i(M, \delta_i) \sin^3 \alpha \right. \\ & \left. + C_{Z_{\alpha^5}}^i(M, \delta_i) \sin^5 \alpha \right] \end{aligned} \quad (9)$$

$$\begin{aligned} M_L^{MAS} = QSD & \left[C_{l_\alpha}^1(M, \delta_1) \sin \alpha + C_{l_\beta}^2(M, \delta_2) \sin \beta \right. \\ & \left. + C_{l_\alpha}^3(M, \delta_3) \sin \alpha + C_{l_\beta}^4(M, \delta_4) \sin \beta \right] \end{aligned} \quad (10)$$

$$\begin{aligned} M_M^{MAS} = QSD & \sum_{i=1}^4 \left[C_{m_\alpha}^i(M, \delta_i) \sin \alpha + C_{m_{\alpha^3}}^i(M, \delta_i) \sin^3 \alpha \right. \\ & \left. + C_{m_{\alpha^5}}^i(M, \delta_i) \sin^5 \alpha \right] \end{aligned} \quad (11)$$

$$\begin{aligned} M_N^{MAS} = QSD & \sum_{i=1}^4 \left[-C_{n_\beta}^i(M, \delta_i) \sin \beta - C_{n_{\beta^3}}^i(M, \delta_i) \sin^3 \beta \right. \\ & \left. - C_{n_{\beta^5}}^i(M, \delta_i) \sin^5 \beta \right] \end{aligned} \quad (12)$$

While the FAS model coefficients are only dependent on Mach number, the MAS aerodynamic model is populated with coefficients that depend on both Mach number and the deflection angle of the i^{th} control surface, δ_i . Both the FAS and MAS coefficients are calculated in the aerodynamic body coordinate frame, with $+X$ out the tail, $+Y$ right, $+Z$ up, as shown in Fig. 3a, and are converted to force and moments in the standard flight dynamics coordinate frame with $+X$ out the nose, $+Y$ right, $+Z$ down, as shown in Fig. 3b, through the formulation of Eqs. 1–12.

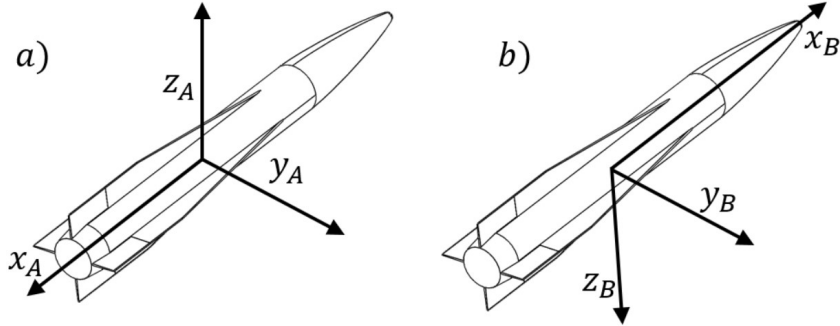


Fig. 3 Comparison of a) the aerodynamic body coordinate frame for the aerodynamic coefficients and b) the flight dynamics coordinate frame for the calculated forces and moments

4. Control Surface Design Methodology

Once the coefficients have been developed to populate the aerodynamic model of the projectile's FAS and MAS, an aerodynamic trim analysis is performed to determine the body angle of attack and lateral acceleration due to varying MAS deflections. This analysis is performed in the pitch plane for vertical accelerations, but represents sideways acceleration capabilities as well due to the pitch and yaw symmetry of the projectile. In this pitch-plane analysis, the individual deflections of flap 1 and flap 3 are combined together following the convention shown in Fig. 2 to produce a pitch deflection, δ_q , as defined in Eq. 13:

$$\delta_q = -\delta_1 + \delta_3 \quad (13)$$

The total pitching moment coefficient, C_m , is calculated from the FAS and MAS models for varying α at each deflection, δ_q . The equilibrium points (trim points) where $C_m = 0$ indicates the steady state α for a given δ_q . This process is illustrated in Fig. 4, which shows projectile trim angles of $[0^\circ, 11^\circ, 19^\circ, 23.5^\circ]$ for δ_q of $[0^\circ, 10^\circ, 20^\circ, 30^\circ]$ at Mach 2, as indicated with red circles.

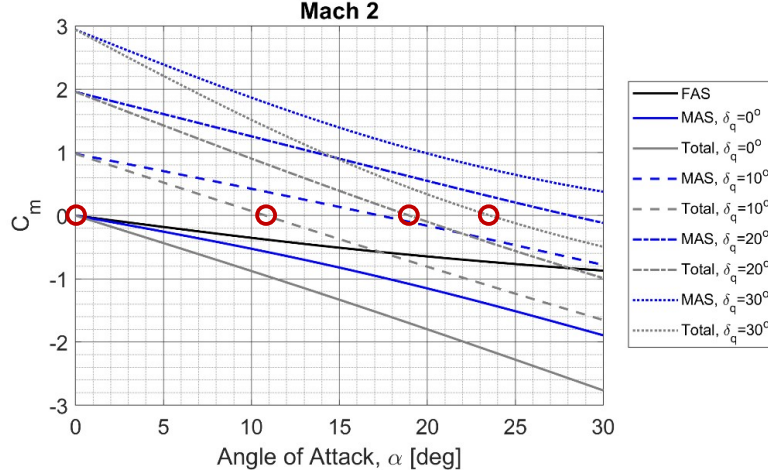


Fig. 4 Total pitching moment, C_m , as well as the FAS and MAS C_m components vs. α for varying δ_q at Mach 2. The pitch trim α for each δ_q is found where the total C_m curves cross the $C_m = 0$ line, indicated with red circles.

Figure 5 plots C_m versus α at Mach 0.6, 1.5, 2, and 3 for the 8-cm control surface. The total combined C_m for the projectile is plotted in gray, with the FAS component shown in black, and the MAS C_m component plotted in blue at different δ_q . Figure 6 plots C_m versus α at Mach 0.6, 1.5, 2, and 3 for the 12-cm control surface, using the same color scheme. In both cases, the projectile is statically stable at subsonic speeds, as indicated by the negative C_m values in Figs. 5a and 6a. As Mach number increases to supersonic, the projectile becomes marginally stable, enabling high α to be achieved using small control surface deflections.

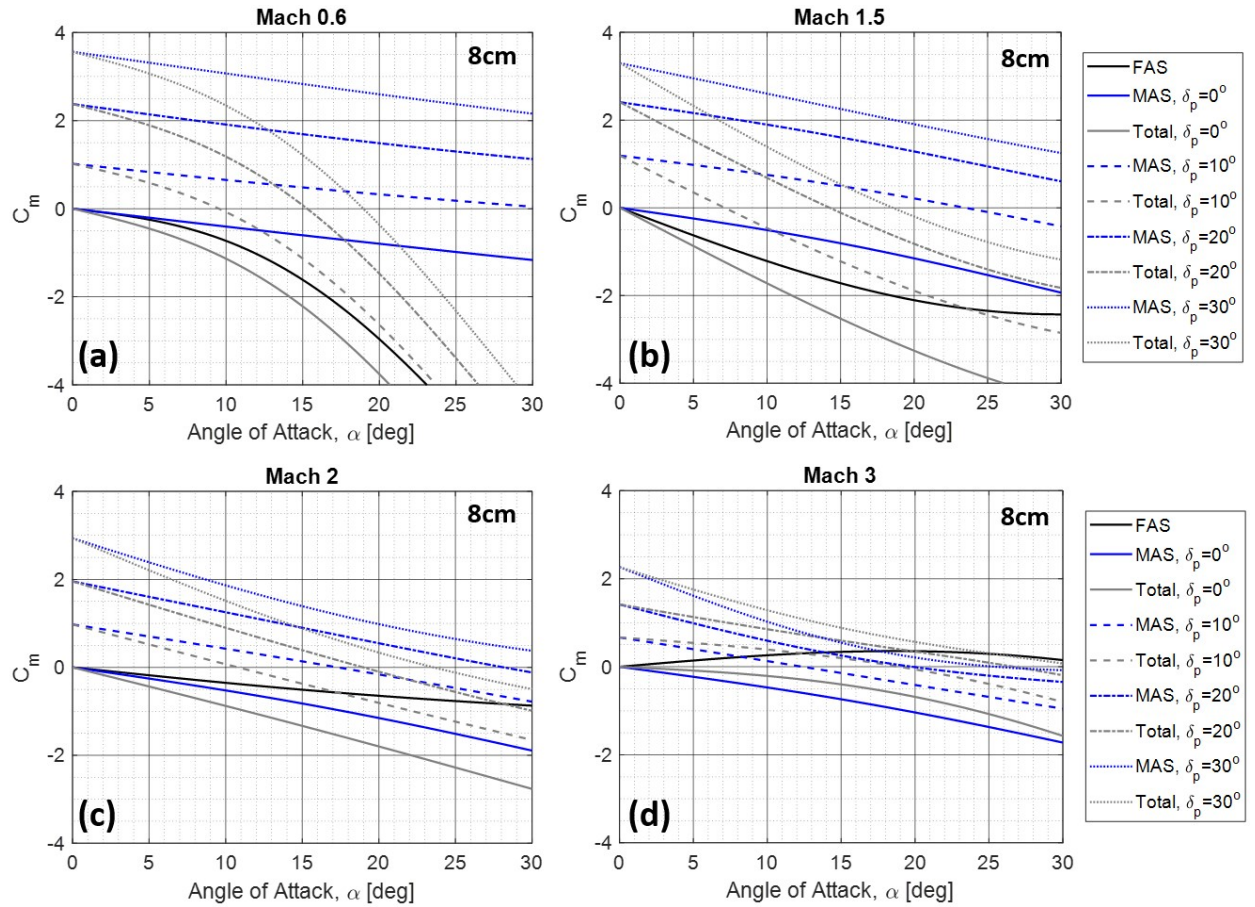


Fig. 5 Total pitching moment, C_m , as well as the FAS and MAS C_m components vs. α for varying δ_q for the 8-cm control surface

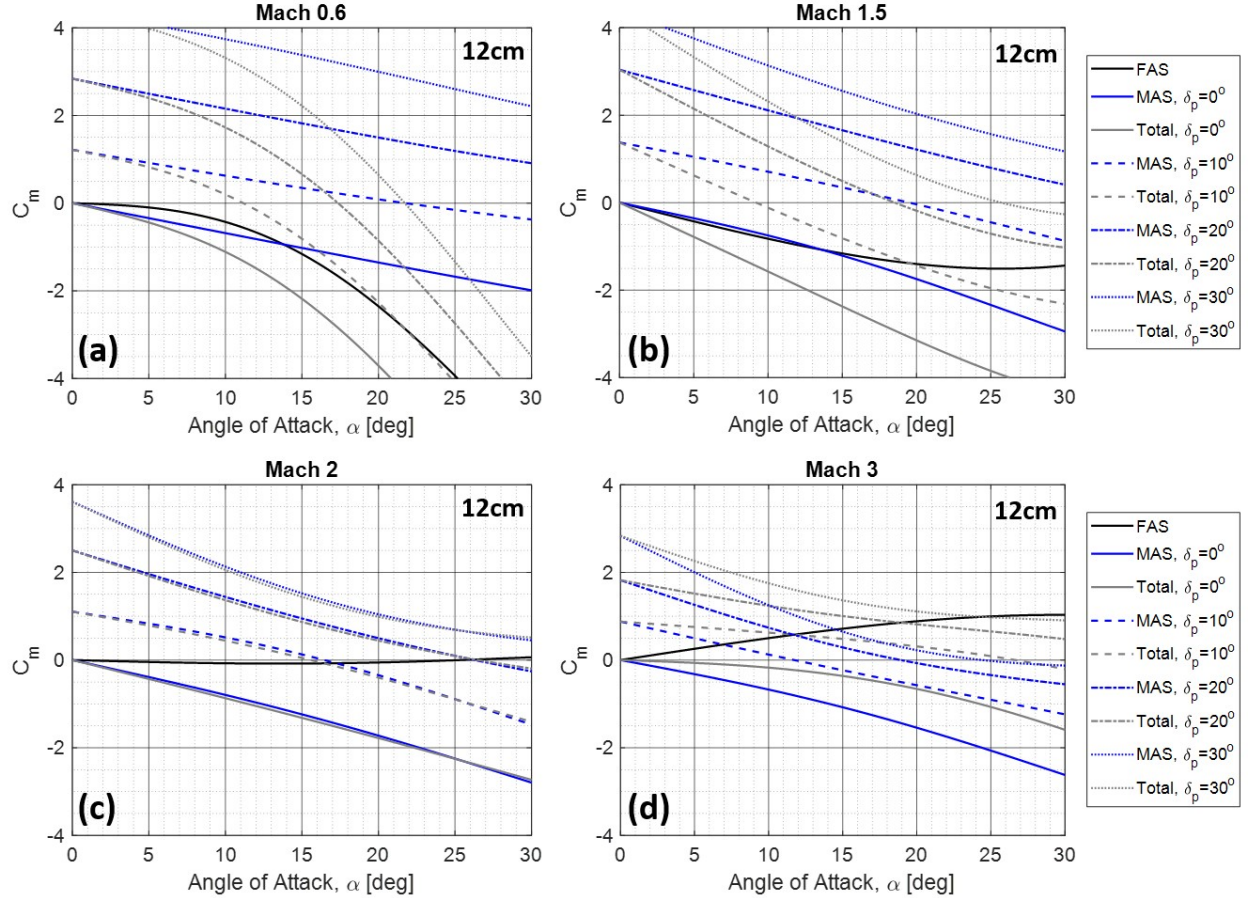


Fig. 6 Total pitching moment, C_m , as well as the FAS and MAS C_m components vs. α for varying δ_q for the 12-cm control surface

The total C_m and C_N data for varying α and δ_q for both the 8- and 12-cm control surfaces are presented using a series of plots in Fig. 7, with constant pitch deflection shown using solid lines and constant attack angle shown using dashed lines. As before, the $C_m = 0$ line indicates the steady-state trim condition for the projectile during flight. Inspecting the intersection between the lines of constant α and constant δ_q along the $C_m = 0$ line shows where the projectile will trim for various deflections, or conversely, what deflection is required to trim at a particular angle of attack. Both control surfaces are sufficient to generate high angles of attack ($\alpha > 10^\circ$) with modest deflections in both supersonic and subsonic flight ($6^\circ - 10^\circ$ at Mach 2; $8^\circ - 12^\circ$ at Mach 0.6). Compared to the 8-cm control surface, the larger 12-cm control surface generates a larger normal force and pitching moment for a given deflection, and as a result requires smaller deflection values to trim at the same angle of attack, as expected.

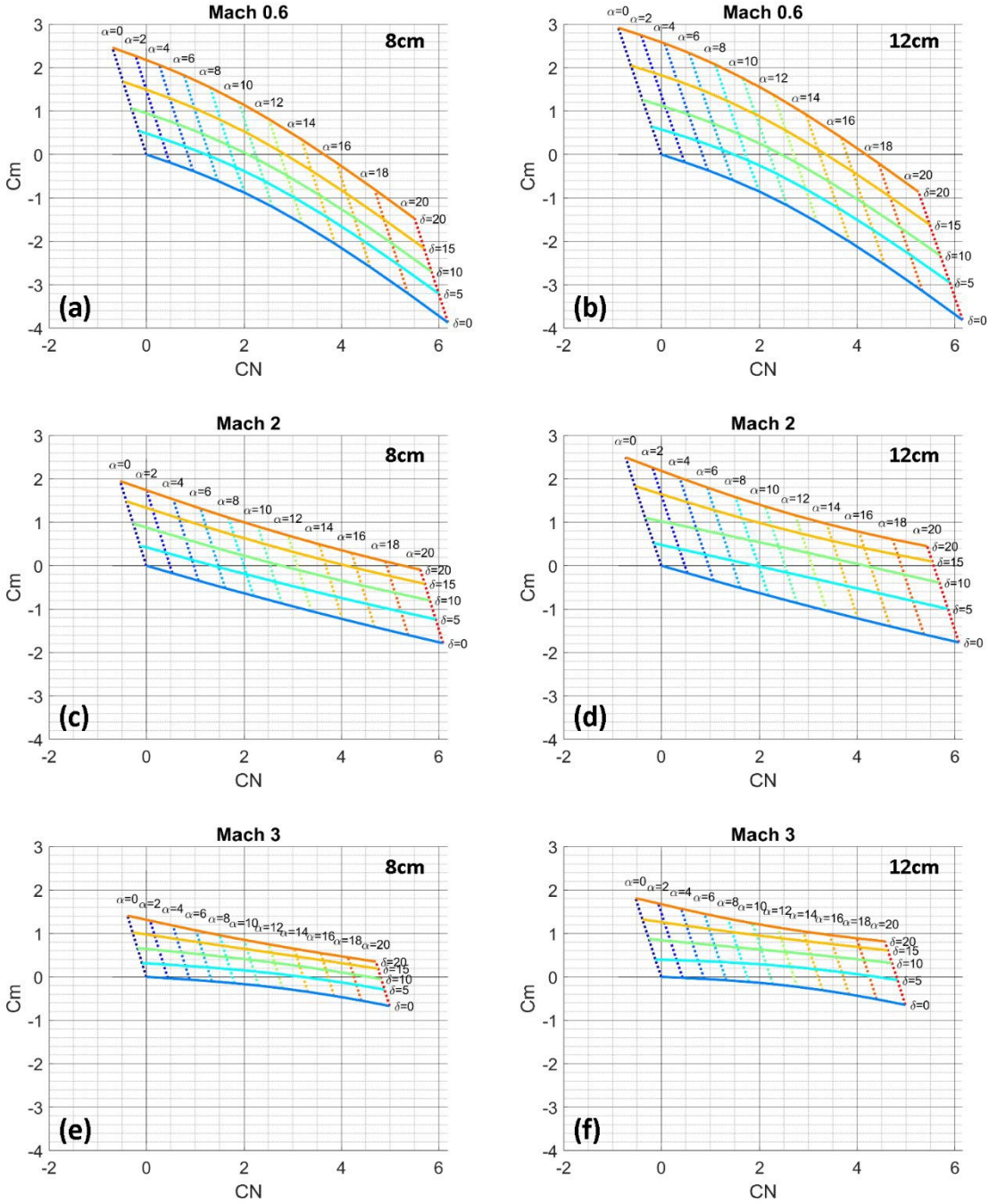


Fig. 7 Total C_m and C_N for 8-cm (a, c, e) and 12-cm (b, d, f) fin-flap data as a function of body angle of attack for α , and pitch deflection, δ , for Mach 0.6 (a, b), 2 (c, d), and 3 (e, f). Lines of constant deflection are solid, while lines of constant angle of attack are dashed.

The lift coefficient, C_L , and drag coefficient, C_D , at α trim is calculated for various δ_q across Mach for the different control surface sizes. Figure 8 shows plots of C_L , C_D , and the lift-to-drag ratio, C_L/C_D . Maximizing C_L/C_D is used as a metric for evaluating performance in this analysis, and the optimal C_L/C_D values across Mach are shown in black on the C_L/C_D plots. The C_L and C_D components comprising the optimal C_L/C_D ratio are also plotted in black on their respective plots. Both control surface designs achieve similar maximum C_L/C_D ratios of about 3 across the supersonic and subsonic flight regimes.

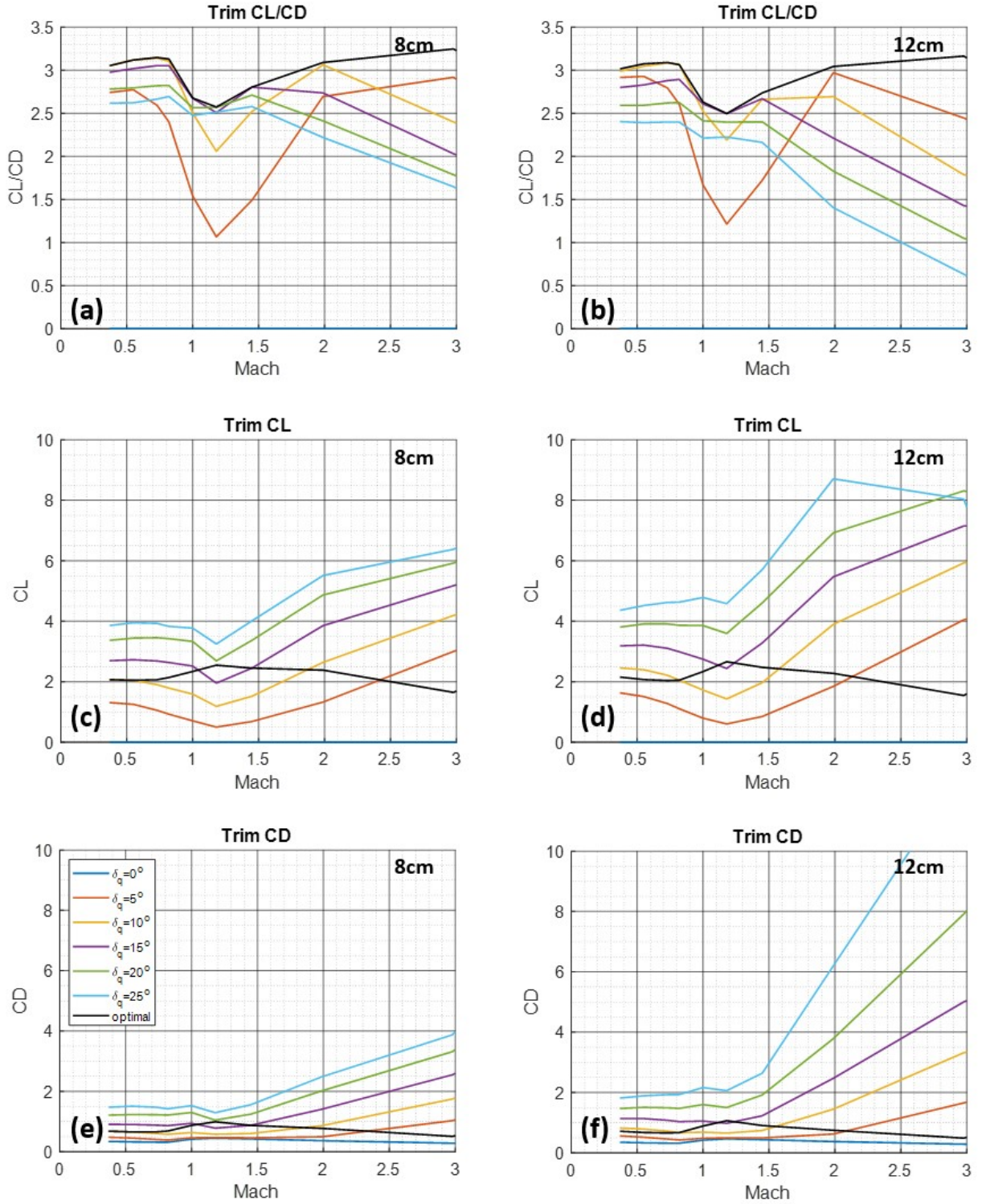


Fig. 8 Comparison of C_L and C_D at trim for various pitch deflections across Mach. The optimal C_L/C_D ratio across Mach is plotted in black in a) and b), with the corresponding C_L and C_D values plotted in black on c), d) and e), f), respectively.

Figure 9 shows how the trim α changes across Mach number for a set of given deflection angles. Note that the lateral force and moment data are calculated using an inviscid flow solver and therefore does not predict flow separation (i.e., onset of stall) accurately; the higher body angles of attack in Figs. 8 and 9 are likely not achievable.

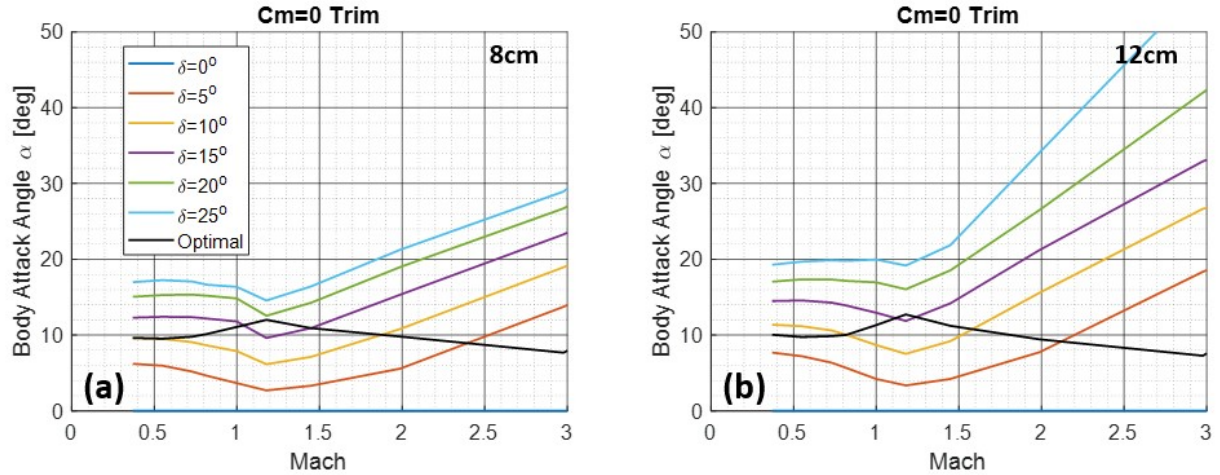


Fig. 9 Trim α across Mach for varying pitch deflection angles for both the 8- and 12-cm control surface. The α corresponding to the maximum lift-to-drag is plotted in black.

Figure 10 facilitates comparisons between the 8- and 12-cm flap designs by plotting each pitch deflection schedule across Mach to achieve the optimal C_L/C_D ratio and the resulting body α . Both the 8- and 12-cm designs achieve similar α for optimal C_L/C_D , but the 12-cm control surface generally requires smaller deflections than the 8-cm design, as expected.

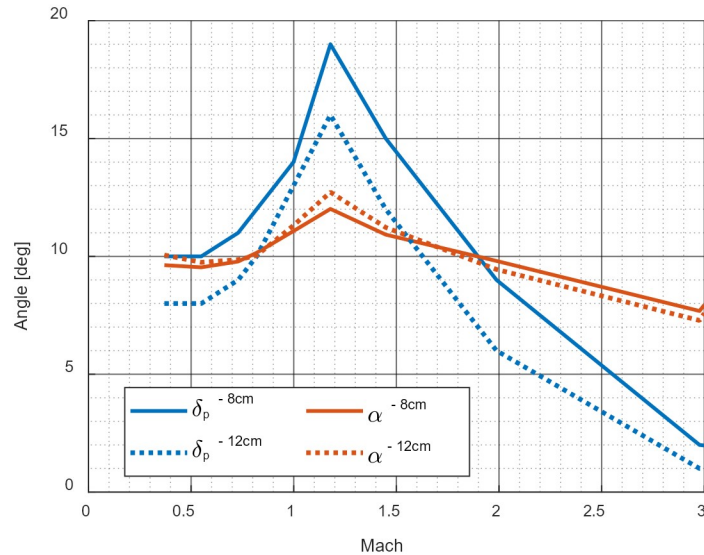


Fig. 10 Pitch deflection schedule across Mach to optimize lift-to-drag ratio for the 8- and 12-cm control surface designs. Both designs achieve similar α to optimize lift-to-drag, but the 12-cm control surface generally requires smaller deflections than the 8-cm design.

5. Conclusion

A methodology was presented to analyze an aerodynamic control surface design and evaluate the effect on a projectile, quantifying the ability to generate lateral accelerations to improve maneuverability, and enabling range extension through glide and terminal maneuvers at both supersonic and subsonic speeds. This control surface analysis methodology facilitates the evaluation of the surface size and effectiveness at achieving a desired angle of attack to generate lift early in the design process, and enables design iterations adjusting aerodynamic stability, static margin, and control surface sizing. This methodology is demonstrated in this report on a gun-launched, aerodynamically stabilized, fin-controlled projectile. Additional aerodynamic studies are also planned, with Navier–Stokes CFD simulations and wind tunnel testing to augment current estimates before beginning flight test evaluations.

6. References

1. Minnicino M, Sorensen B, Hepner DJ, Horst AW, Schmidt EM, Brandon FJ. Artillery range extension. Aberdeen Proving Ground (MD): Army Research Laboratory (US); 2010 June. Report No.: ARL-TR-5221.
2. Costello M. Extended range of a gun launched smart projectile using controllable canards. Shock Vib. 2001;8(3–4):203–213.
3. Fresconi FE. Range extension of gun-launched smart munitions. In: Bless S, editor. Proceedings of 24th International Symposium on Ballistics; 2008 Sep 22–26; New Orleans, LA. Lancaster (PA): DEStech Publications, Inc.; c2008. pp. 157–164.
4. Bryson JT, Vasile JD, Celmins I, Fresconi FE. Approach for understanding range extension of gliding indirect fire munitions. Reston (VA): AIAA SciTech. 2018;3158.
5. Vasile JD, Bryson JT, Fresconi FE. Aerodynamic design optimization of long range projectile using missile DATCOM. Reston (VA): AIAA SciTech. 2020;1762.
6. Rosema C, Doyle J, Blake W. Missile DATCOM user's manual – 2014 revision. Wright Patterson Air Force Base (OH): Flight Dynamics Directorate, Air Force Research Laboratory (US); 2014 Dec. Report No.: AFRL-RQ-WP-TR-2014-0281.
7. Aftosmis MJ, Berger MJ, Adomavicius G. A parallel multilevel method for adaptively refined Cartesian grids with embedded boundaries. 38th Aerospace Sciences Meeting and Exhibit; 2000 Jan 10–13; Reno, NV. Reston (VA): American Institute of Aeronautics and Astronautics, Inc.; AIAA-2000-0808.
8. McCoy RL. Modern exterior ballistics. Atglen (PA): Schiffer; 2012.
9. Fresconi FE, Celmins I, Silton S, Costello M. High maneuverability projectile flight using low cost components. Aerosp Sci Technol. 2015;41:175–188.
10. Zipfel PH. Modeling and simulation of aerospace vehicle dynamics. AIAA Education Series. Reston (VA): American Institute of Aeronautics and Astronautics, Inc.; 2014.
11. Fresconi FE, Celmins I, Maley J, Nelson B. Experimental flight characterization of a canard-controlled, subsonic missile. Aberdeen Proving Ground, (MD): Army Research Laboratory (US); 2017 Aug. Report No.: ARL-TR-8086.

12. Bryson JT, Vasile JD, Gruenwald BC, Fresconi FE. Control surface design analysis and actuation requirements development for munitions. Reston (VA): AIAA SciTech. 2020;0020.
13. Vasile JD, Bryson JT, Gruenwald BC, Fairfax L, Strohm L, Fresconi FE. A multi-disciplinary approach to evaluate long range guided projectiles. Reston (VA): AIAA SciTech. 2020;1993.

Nomenclature

α	=	body angle of attack in pitch plane
$\bar{\alpha}$	=	total body angle of attack, $\sqrt{\alpha^2 + \beta^2}$
β	=	body angle of sideslip in yaw plane
C_D	=	drag coefficient
C_L	=	lift coefficient
C_{l_0}	=	zeroth order roll moment coefficient
C_{l_p}	=	roll damping coefficient
C_m	=	coefficient of pitching moment
$C_{m_\alpha}, C_{m_{\alpha^3}}, C_{m_{\alpha^5}}$	=	first, third, and fifth order fit coefficients for aerodynamic pitching moment
C_{m_q}	=	pitch damping coefficient
$C_{n_\beta}, C_{n_{\beta^3}}, C_{n_{\beta^5}}$	=	first, third, and fifth order fit coefficients for aerodynamic yaw moment
C_{n_r}	=	yaw damping coefficient
$C_{X_0}, C_{X_{\bar{\alpha}^2}}$	=	zeroth, and second order fit coefficients for X-axis aerodynamic force
$C_{Y_\alpha}, C_{Y_{\alpha^3}}, C_{Y_{\alpha^5}}$	=	first, third, and fifth order fit coefficients for Y-axis aerodynamic force
$C_{Z_\alpha}, C_{Z_{\alpha^3}}, C_{Z_{\alpha^5}}$	=	first, third, and fifth order fit coefficients for Z-axis aerodynamic force
$\delta_1, \delta_2, \delta_3, \delta_4$	=	deflection angles for control surface 1,2,3,4
δ_q	=	deflection of virtual/combined control surface for pitch
D	=	reference diameter
M	=	Mach number
Q	=	$\frac{1}{2} \rho V^2$, dynamic pressure
S	=	$D^2 \pi / 4$, aerodynamic reference area

List of Symbols, Abbreviations, and Acronyms

CFD	computational fluid dynamics
FAS	fixed aerodynamic surfaces
MAS	movable aerodynamic surfaces
NASA	National Aeronautics and Space Administration

1 DEFENSE TECHNICAL
(PDF) INFORMATION CTR
DTIC OCA

1 CCDC ARL
(PDF) FCDD RLD CL
TECH LIB

15 CCDC ARL
(PDF) FCDD RLW LE
J BRYSON
J VASILE
FCDD RLW A
F FRESCONI
FCDD RLW L
T SHEPPARD
W OBERLE
FCDD RLW LE
I CELMINS
J DESPIRITO
B GRUENWALD
L FAIRFAX
L STROHM
FCDD RLW LB
N TRIVEDI
FCDD RLW LC
J SADLER
FCDD RLW LD
P CONROY
FCDD RLW LF
M ILG
FCDD RLW LH
J NEWILL